Large local optical activity in fractal aggregates of nanoparticles

Vladimir P. Drachev,* W. David Bragg,† Viktor A. Podolskiy, Vladimir P. Safonov,†† Won-Tae Kim, Z. Charles Ying, Robert L. Armstrong, and Vladimir M. Shalaev†††

Department of Physics, New Mexico State University, Las Cruces, New Mexico 88003

Received December 12, 2000; revised manuscript received April 19, 2001

Large *local* optical activity in fractal aggregates of silver nanoparticles has been observed by means of photon scanning tunneling microscopy. The effect occurs because resonant plasmon modes in random fractals can have handedness in spatial distribution of their amplitudes. In agreement with experimental observations, numerical simulations show dramatic difference in dipole-moment distributions for right- and left-circularly polarized incident light when the cluster size is comparable with or larger than the wavelength. Variations in the local parameter describing the circular intensity difference of scattered light show that fractal aggregates are characterized by broad and random distributions of chiral plasmon modes. © 2001 Optical Society of America

OCIS codes: 240.6680, 290.5880.

1. INTRODUCTION

Recently a number of intriguing optical phenomena, including localization of optical excitations and dramatically enhanced optical nonlinearities, have been predicted and observed for fractal objects.[1–6] The localization in fractals results from their scale-invariant morphology, which does not support the propagating waves typical for translationally invariant systems. The localization is inhomogeneous in the sense that eigenmodes with different coherence lengths can coexist at the same frequency.[7] Optical excitations in fractals are not uniformly distributed but rather concentrated in hot spots much smaller in size than the size of the fractal cluster and often the wavelength as well. The strong electromagnetic fields in these hot spots can result in large enhancement of optical nonlinearities and other effects that require intense fields. In fractal aggregates composed of metal nanoparticles, the optical excitations are associated with plasmon modes, which can have high resonance quality factors and thus provide particularly strong enhancement in the hot spots.[2–4,6]

The localized optical modes of fractals have been studied by use of photon scanning tunneling microscopy (PSTM) with subwavelength spatial resolution.[8–10] The technique is effective for linear and nonlinear optical imaging of a variety of smooth and rough surfaces.[11,12] It has been shown that hot-spot locations are very sensitive to even small changes in linear polarization plane and frequency of the applied field (~1% in the latter case).[8–10]

The observed linear polarization dependence, in particular, illustrates strong local anisotropy of plasmon modes in fractals. However, an important question, whether the fractal optical modes exhibit handedness, to our knowledge has not been addressed so far. It is known, for example, that two coupled anisotropic oscillators lying in different planes represent a simple model of a chiral system. Fractal aggregates are formed by chains of particles with almost all possible local configurations. These local structures have typically neither center nor plane of symmetry and thus may have handedness so that a fractal mode localized on such a structure exhibits chirality. Thus one may anticipate that the fractal modes can be chiral active and manifest *locally* the property of optical activity. Studies of chiral properties of plasmon modes are additionally motivated by recent observation of nonlinear gyrotropy in macroscopic samples of silver nanocomposites.[13]

Optical activity is characterized by different responses to right- and left-circularly polarized light. Optical activity phenomena include differences in attenuation (circular dichroism), refraction (circular birefringence), and scattering for right- and left-circularly polarized light. Scattering optical activity is denoted as circular intensity differential scattering (CIDS).[14] In previous studies, only *macroscopic* optical activity was considered.[14] However, macroscopic effects are significantly reduced for a racemic mixing of chiral elements (approximately equal amounts of elements with opposite handedness). Therefore the local optical activity detected with PSTM may be much stronger than typically observed macroscopic effects and provides important information on chirality of local structures and their statistical properties.

In this paper we report experimental observation and theoretical simulation of giant local CIDS in fractal aggregates of silver colloidal particles, thereby providing the first evidence that plasmon excitations in fractals are optically active. With the aid of PSTM one can study the *local* chirality of small nanostructures, provided there is strong enhancement of optical responses, which occurs in fractals and possibly in other structures.

2. EXPERIMENTS

Preparation of fractal aggregates and details of our PSTM apparatus are published elsewhere.[6,15] Here, we outline

only the most important steps. Solutions of silver colloid particles of ~10 nm in size were prepared by a citrate reduction method.[16] The addition of organic adsorbate promoted aggregation of colloidal particles into fractal clusters. Roughly 2μl of the fractal aggregate solution was deposited onto a glass substrate, resulting in a thin layer of fractal material; atomic force microscopy measurements showed that the thickness of this layer was ~100 nm. The density of the deposited fractals was roughly 5×10^6 per cm^2. A transmission electron microscopy image of a sample prepared in this way (Fig. 1) clearly indicated the fractal structure of the aggregates, which have fractal dimension $D \approx 1.75$. The fractal dimension was determined by use of the relation $N \sim (R/R_0)^D$, where N is the number of monomers in the aggregate of gyration radius R, and R_0 is the monomer size. Fractal aggregates, typically consisting of several thousand monomers, have sizes of 1 to 3 μm. The resonance spectra of individual silver particles and their aggregates, and the deposition-caused transformation of self-similar aggregates into self-affine structures, with similar optical properties, are described in detail elsewhere.[6,9,10]

Fractal colloidal aggregates were placed, with index-matching fluid, on the hypotenuse face of a 90° prism and illuminated by an evanescent field in the total internal reflection geometry (see Fig. 2). The illumination source was either a helium–neon laser operating at a wavelength of 633 nm or a tunable diode laser (Newport 2010) operating between 790 and 820 nm. The polarization of the beam was controlled with a Glan–Thompson polarizer (New Focus 5524) and a variable wave plate (New Focus 5540). The local optical signal was collected through an uncoated optical fiber, sharpened to approximately 50-nm radius at its tip by a fiber puller (Sutter Instruments P-2000). The separation between the probe tip and the sample was regulated with nonoptical shear-force feedback when the PSTM was operating in the constant-height mode. Alternatively, the sample was scanned in a constant plane above the sample without active feedback for the probe height.

Figures 3(a) and 3(b), which were obtained with the microscope operated in the constant height mode, show the local optical images of the fractal sample for right- and left-circularly polarized incident light, respectively. Both images exhibit large variations of light intensity and many hot spots. Visual examination of the two images reveals different spatial distributions of hot spots for the two polarizations, indicating circular differential response in certain regions. The topographic images recorded simultaneously with the optical images are shown in Figs. 3(c) and 3(d). The topographic images ensure that the optical images with different circular polarizations were recorded at the same area.

In order to reduce tip wear and sample damage over the long experiment and to prevent a random bent of the fiber tip in the shear-force contact with the surface, the microscope was operated under the constant-plane mode in our detailed studies of polarization and wavelength dependence. Comparison of the PSTM images obtained in the two modes demonstrated the absence of topographically induced artifacts that were described in previous publications.[17,18] It should be noted that the scanning

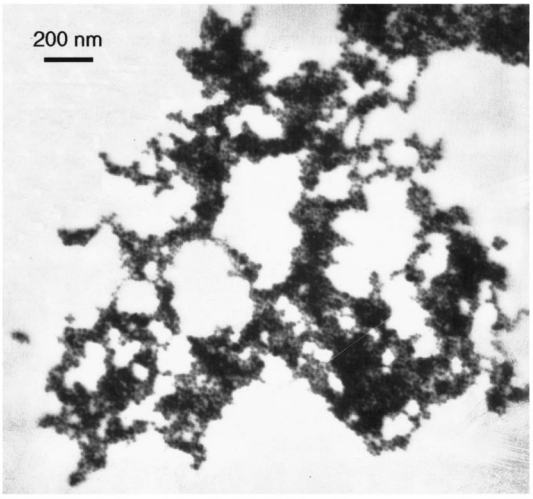

Fig. 1. TEM image of silver fractal aggregates.

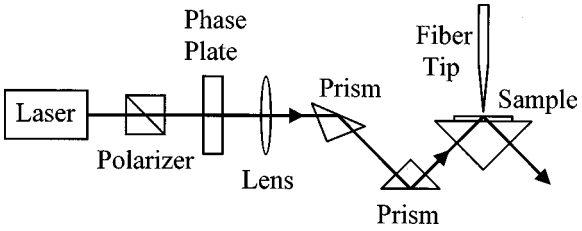

Fig. 2. Experimental setup.

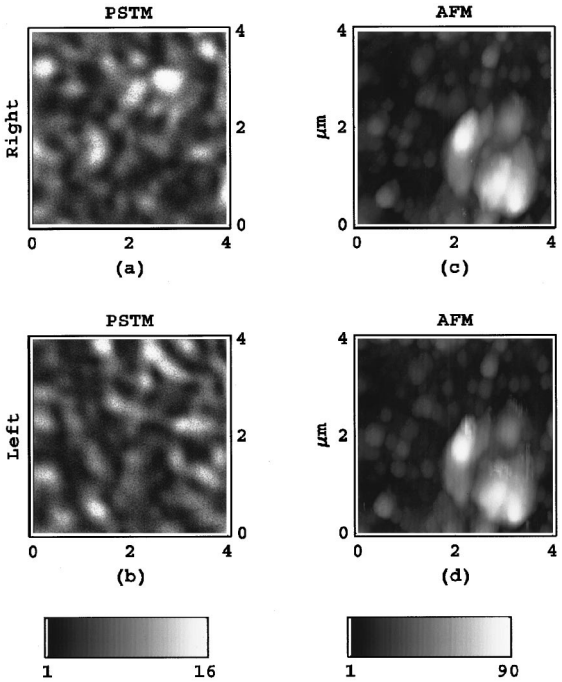

Fig. 3. PSTM images of silver fractal aggregates with (a) right- and (b) left-circularly polarized incident light at 633 nm. The microscope was operated in the constant-height mode with the shear-force feedback, and the topographic images recorded simultaneously are shown in (c) and (d), with depth ranging from 1 to 90 nm. Each image is 4 μm × 4 μm in size.

plane in our apparatus was tilted by approximately 14° with respect to the sample surface, and consequently the tip height changed from ~100 nm to ~2400 nm during a 10 μm × 10 μm scan in the constant-plane mode. The experimental images recorded in the constant-plane mode, shown in Fig. 4, exhibit quite uniform lateral size and contrast of hot spots (i.e., spatial regions of very high intensity shown in white) over the whole imaging area despite the fact that the images were recorded with varying tip heights. In addition, the images obtained in the constant-plane mode show approximately the same spot sizes and contrast as in the constant-height mode [Figs. 3(a) and 3(b)]. These observations indicate that the size of hot spots is preserved when the tip–sample distance varies from tens of nanometers to a few micrometers; there is also no strong dependence of the optical signal on the tip height, in agreement with PSTM studies by other authors.[19,20]

The weak distance dependence is likely a result of the use of an uncoated fiber tip, where the light enters the fiber from both the tip end itself and the side wall near the tip end. We estimated that only the light incident on the side wall within an acceptance distance of 2–4 μm from the tip end and within an acceptance angle of approximately 3° (the same as the numerical aperture of a single-mode fiber) was collected by the fiber. Our numerical simulations with this collection geometry showed preservation of subwavelength hot-spot size at tip heights up to several micrometers and a relatively weak dependence of the average optical signal on the tip height. The observed weak tip–sample dependence means that the light scattered by our sample contributes mainly to the collected signal. The average size of hot spots determined from autocorrelation function (Fig. 5) is of the order of 400 nm. It gives the upper limit for lateral resolution of our measurements.

Figures 4(a) and 4(b) show the local optical images of the fractal sample for right- and left-circularly polarized incident light, respectively, with the microscope operated in the constant-plane mode. These images exhibit qualitatively similar results as those recorded in the constant-height mode. The weak correlation of the two images is confirmed by a correlation analysis as illustrated in Fig. 5, where the cross-correlation function $g_c(\mathbf{R}) = C_1[\langle I_L(\mathbf{r})I_R(\mathbf{r}+\mathbf{R})\rangle - \langle I_L(\mathbf{r})\rangle\langle I_R(\mathbf{r})\rangle]$ and autocorrelation function $g_{ac}(\mathbf{R}) = C_2[\langle I_{L,R}(\mathbf{r})I_{L,R}(\mathbf{r}+\mathbf{R})\rangle - \langle I_{L,R}(\mathbf{r})\rangle^2]$ for the two images are shown. The normalization constants C_1 and C_2 are chosen so that $g_{ac}(0) = 1$, and, if the intensities of scattered light had been equal for the two circular polarization inputs, $g_c(0) = 1$. The autocorrelation functions for the right- and left-circularly polarizations (solid curves in Fig. 5) are essentially the same, indicating that, *on average*, the field distributions are almost identical for the two circular polarizations. The autocorrelation functions are, however, very different from the cross-correlation function of the two images (squares in Fig. 5), which is close to zero even at small distances R, indicating nearly no correlation in the intensity distribution for the two circular polarizations.

Control PSTM measurements on samples of nonaggregated particles reveal no hot spots, showing instead a uniform field distribution. This observation indicates that the effect described above is related to the fractal sample itself.

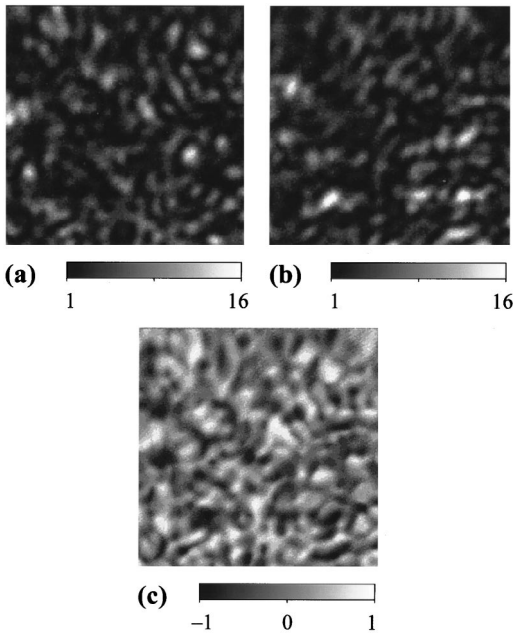

Fig. 4. PSTM images of silver fractal aggregates with (a) right- and (b) left-circularly polarized incident light at 633 nm. The microscope was operated in the constant-plane mode without the shear-force feedback. (c) Local CIDS signal computed from the optical images (see the text for details). Each image is 10 μm × 10 μm in size.

It is instructive to consider scattering of an incident evanescent wave by surface fractal structures in terms of the Mueller scattering matrix $S_{\alpha\beta}(\alpha, \beta = 1, 2, 3, 4)$, which relates the Stokes vectors of the scattered wave, W_α, and the incident wave, W_β, as $W_\alpha = S_{\alpha\beta}W_\beta$.[21] Let E_s and E_p be s- and p-polarized components of the wave (electric field perpendicular and parallel to the plane of incidence). Its four Stokes parameters are $I = E_sE_s^*$

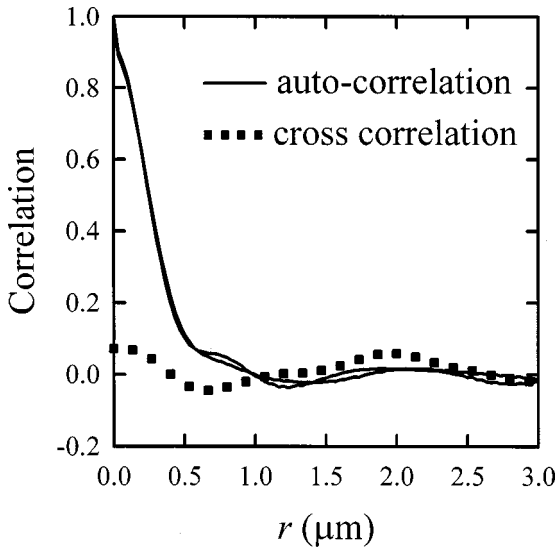

Fig. 5. Cross-correlation (squares) and autocorrelation (solid curves) functions computed from the two images shown in Figs. 4(a) and 4(b).

$+ E_pE_p^*$, $Q = E_sE_s^* - E_pE_p^*$, $U = E_sE_p^* + E_pE_s^*$, and $V = i(E_sE_p^* - E_pE_s^*)$. The first Stokes parameter I gives the light intensity. For equal intensities in the s- and p-polarized components, i.e., for $|E_s| = |E_p|$, the Stokes vector becomes $I(1; 0; \cos\delta, \sin\delta)$, where $I = |E_s|^2 + |E_p|^2$ and $\delta = \delta_p - \delta_s$ is the phase difference between the two components. Note that $I(1; 0; \pm 1; 0)$ ($\delta = 0$ or π) corresponds to linear polarization and $I(1; 0; 0; \pm 1)$ ($\delta = \pm\pi/2$) corresponds to right- and left-circular polarizations, respectively.

It should be emphasized that the incident waves used in our experiments are evanescent waves created near the hypotenuse face of the prism by the total internal reflection. The wave amplitude decays exponentially in the $\hat{z}$ direction that is normal to the hypotenuse face,

$$\mathbf{E}_{ev} = \frac{1}{\sqrt{2}} E_0 \exp(-\gamma z)[\hat{y}\cos(k_x x - \omega t) + \hat{z}\cos(k_x x - \omega t - \delta)], \quad (1)$$

where $\gamma = (\omega/c)\sqrt{n^2\sin^2\theta - 1}$ and $k_x = (\omega/c)n\sin\theta$ depend on the prism's refractive index n and angle of incidence θ. Note that the phase difference δ has two sources: an initial value δ_0 due to the incident plane wave (controlled by the variable wave plate) and an additional contribution δ_f because of the total internal reflection at the hypotenuse face of the prism, $\delta = \delta_0 + \delta_f$. If we denote E_s and E_p as the amplitudes of evanescent waves in the s and p directions, respectively, and $E_{s,i}$ and $E_{p,i}$ as the corresponding amplitudes of incident plane waves, these quantities are related by $E_s/E_p = \alpha\exp(i\delta_f)(E_{s,i}/E_{p,i})$. The expressions for δ_f and α are determined from the Fresnel formulas:

$$\tan\delta_f = \frac{\cos\theta\sqrt{n^2\sin^2\theta - 1}}{n\sin^2\theta}, \quad (2)$$

$$\alpha = \sqrt{n^2\sin^4\theta + \cos^2\theta(n^2\sin^2\theta - 1)}. \quad (3)$$

For a refractive index of $n = 1.52$ and an incident angle of $\theta = 49°$, as used in our experiments, $\delta_f \approx \pi/8$ and $\alpha^2 \approx 0.9$. The intensities of the incident plane wave along the s and p two directions were adjusted to achieve equal intensity in the evanescent wave.

The intensity of the scattered wave, under the condition $|E_s| = |E_p|$ for the incident evanescent wave, is given by

$$I(\mathbf{r}, \delta) = I_0\exp(-2\gamma z) \times [S_{11}(\mathbf{r}) + S_{13}(\mathbf{r})\cos\delta + S_{14}(\mathbf{r})\sin\delta]. \quad (4)$$

Parameters S_{13} and S_{14} characterize anisotropy and optical activity, respectively. The scattered intensities for right- and left-circularly polarized incident light are given by $I_{R,L} = I_0\exp(-2\gamma z)(S_{11} \pm S_{14})$. The dimensionless parameter that describes CIDS is $S_{14}/S_{11} = (I_R - I_L)/(I_R + I_L)$.[14,21]

Seventeen optical images with $\delta = n\pi/8$ and $n = 0, 1, 2, \ldots, 16$ were recorded for each (He–Ne or diode laser) wavelength to study optical activity and anisotropy. The phase difference δ was controlled by a variable wave plate. We have also taken into account the phase shift due to the total internal reflection.

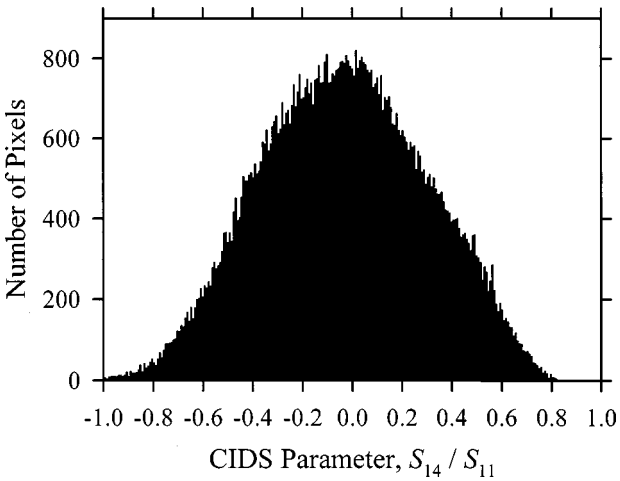

Fig. 6. Histogram for local CIDS parameter.

Two methods were used to obtain the CIDS parameter $S_{14}(\mathbf{r})$. While the CIDS parameter can be computed by use of only two images with $\delta = \pi/2$ and $3\pi/2$ [Figs. 4(a) and 4(b)], the entire phase dependence at each point from all 17 images was used in computation of the CIDS parameter with the least-squares fit to Eq. (4), which provides higher statistical credibility for the data analysis. Both methods give nearly the same results.

Figure 4(c) shows distribution for the local CIDS parameter $(I_R - I_L)/(I_R + I_L)$ computed from 17 optical images. The white and black spots in Fig. 4(c) represent areas of preferential scattering for right- and left-circularly polarized incident light, respectively. The variations in the parameter CIDS demonstrate that fractal aggregates are characterized by a broad and random

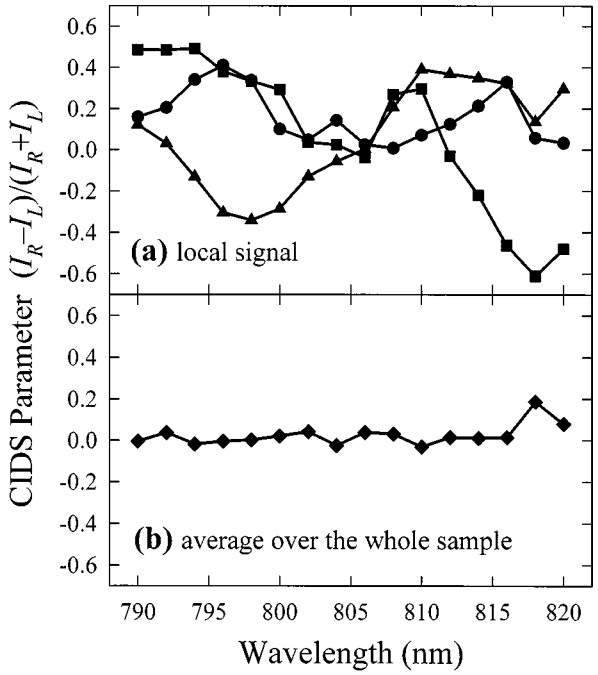

Fig. 7. Wavelength dependence of (a) local (at three different spatial positions) and (b) average CIDS parameters for silver fractal aggregates.

distribution of chiral elements associated with the plasmon modes. The randomness is characterized by a histogram for the number of pixels sorted in accordance with the CIDS sign and value, as shown in Fig. 6. The distribution is broad, with the half-width at the half-maximum being ~0.45. Despite weak asymmetry, the histogram shows approximately equal numbers of chiral areas with opposite handedness.

Figure 7(a) exhibits wavelength dependence of the local CIDS parameter at three different spatial positions, each of which is a location of a hot spot at a wavelength for at least one of the two circular polarizations. The local optical activity is large ($|(I_R - I_L)/(I_R + I_L)|$ up to 0.6) and varies strongly with wavelength. The sign of $(I_R - I_L)/(I_R + I_L)$ can change, even for very small changes of wavelength, ~10 nm. In sharp contrast the value of the CIDS parameter averaged over the whole 10 × 10 μm sample shown in Fig. 7(b) is much smaller: $|(I_R - I_L)/(I_R + I_L)| = 0.026 \pm 0.045$. The macroscopic absorption spectra of our samples have a flat wavelength dependence in this range, with no spectral structures. All these results clearly show that, while locally there exist areas of strong preference for scattering of one circular polarization or the other, this preference is effectively absent when averaged over a macroscopic sample. This result opens new avenues in optical activity studies where *local* gyrotropy effects may be investigated with photon scanning tunneling microscopy.

3. NUMERICAL SIMULATIONS AND DISCUSSIONS

We simulated our observations numerically by use of a model that realistically describes a fractal aggregate deposited on a surface.[9,10] The system is described by the coupled-dipole equations (CDEs), whose numerical solution permits the determination of dipoles $\mathbf{d}_i$ located at $\mathbf{r}_i$ and field distribution $\mathbf{E}(\mathbf{r})$. Elementary dipoles associated with nongyrotropic particles in a fractal aggregate interact with the incident evanescent field and with each other through the dipolar fields, which are established self-consistently. Higher-multipole contributions are taken into account by introducing the effective intersecting spheres.[22–24]

Solution to the CDEs can be represented in terms of an expansion over the eigenvectors $|n)$ of the dipolar operator: $V|n) = v_n|n)$;[23,25] the operator V includes the near-, intermediate-, and far-zone terms for the dipole field (see also Ref. 6). The dipoles induced by the circularly polarized incident field

$$\mathbf{E}_{R,L} = E_0 \hat{\boldsymbol{\sigma}}_{R,L} = E_0 \exp(-\gamma z)\frac{\hat{y}\cos(k_x x - \omega t) \pm \hat{z}\sin(k_x x - \omega t)}{\sqrt{2}} \tag{5}$$

are expanded over the eigenmodes as

$$(d_{i\alpha})_{R,L} = \sum_n (i\alpha|n)[(\bar{n}|n)]^{-1}(\alpha_0^{-1} + v_n)^{-1}(\bar{n}|\,\sigma_{R,L})E_0, \tag{6}$$

where α denotes the Cartesian components and α_0 is the polarizability of individual particles. In this expansion,

$$(\bar{n}|\,\sigma_{R,L}) = \sum_j \exp(-\gamma z_j)[(\bar{n}|jy)\cos(k_x x_j - \omega t) \pm (\bar{n}|jz)\sin(k_x x_j - \omega t)]/\sqrt{2}$$

represents the projection of the mode vector on the circular-polarization vector of the inhomogeneous wave and an orthogonal basis $|i\alpha)$ is defined in $3N$-dimensional complex vector space. Vector $(\bar{n}|$ is a row vector with the same entries as a column vector $|n)$, as opposed to $(n|$, which is a row vector with the complex-conjugated elements.[25] Note that for a given mode, the polarization dependence is contained in the projection of the mode on the incident field $(\bar{n}|\,\sigma_{R,L})$.

The difference in optical responses to different circular polarizations occurs because the fractal modes may have different projections $(\bar{n}|\,\sigma_{R,L})$ on the helical configuration of the incident field with opposite signs of helicity. In other words, the spatial distribution of a fractal eigenmode can have handedness, and in that sense they possess chirality. As mentioned, this mode chirality is possible because local structures in a fractal typically have neither center nor plane of symmetry. This leads to different distributions for dipole moments and, as a consequence, to different optical responses for right- and left-circular polarizations.

The absorption cross section per ith particle can be expressed through the dipole moment as[25]

$$(\,\sigma_a)_{iR,L} = \frac{4\pi k}{|E_0|^2} y_a \sum_\alpha |d_{i\alpha}|^2_{R,L}, \tag{7}$$

where constant $y_a = -\mathrm{Im}(\alpha_0^{-1}) - 2k^3/3$ is nonnegatively defined for any physically reasonable α_0, and it characterizes the absorption by a single isolated particle. The dipole-moment distribution is given by

$$|d_{i\alpha}|^2_{R,L} = \sum_{n,m} n_{i\alpha} m^*_{i\alpha} C_n C^*_m \sum_{j,l} \exp[-\gamma(z_j + z_l)][(n_{jy}m^*_{ly} + n_{jz}m^*_{lz})\cos k_x(x_j - x_l) \pm (n_{jz}m^*_{ly} - n_{jy}m^*_{lz})\sin k_x(x_j - x_l)](E_0^2/4), \tag{8}$$

where $n, m = 1,\ldots,3N$ numerate the modes, and $j, l, i = 1,\ldots,N$ numerate the particles; for simplicity the mode amplitudes $(i\alpha|n)$ are denoted as $n_{i\alpha}$ and the resonance constant of the nth mode as $C_n \equiv [(\bar{n}|n)]^{-1}(\alpha_0^{-1} + v_n)^{-1}$. The circular difference can be characterized by

$$\Delta|d_{i\alpha}|^2_{R,L} = \sum_{n,m} n_{i\alpha} m^*_{i\alpha} C_n C^*_m \sum_{j,l} \exp[-\gamma(z_j + z_l)] \times (n_{jz}m^*_{ly} - n_{jy}m^*_{lz}) \times \sin k_x(x_j - x_l)(E_0^2/2), \tag{9}$$

and it increases with increasing the anisotropy factor $(n_{jz}m^*_{ly} - n_{jy}m^*_{lz})$ and cluster size through a geometrical factor $\sin k_x(x_j - x_l)$.

Equation (9), as well as the numerical simulations, suggest that the local optical activity in fractals, as in any other systems, is directly related to spatial-dispersion ef-

fects in particle–particle interactions. Figure 8 shows the dipole distribution for a model fractal cluster containing 5000 particles of 20-nm size. This distribution was computed by numerically solving the CDEs. We can see a dramatic difference between the optical responses to left- and right-circular polarized light, i.e., strong optical activity. In accordance with Eq. (9) this implies both a large anisotropy factor and large sizes (comparable with $\lambda/4$) occupied by some plasmon modes.

To investigate the role of cluster size in optical activity we purposely decreased the size of the simulated fractal used in Fig. 8 by 100 times. The dipole-moment distribution for the compressed fractal is shown in Fig. 9. As expected, the elimination of the spatial-dispersion effects (by taking the size of the system to be much smaller than the wavelength) removes the circular difference in the dipole distribution.

We should emphasize that the cluster-size effect manifests itself only in *nonlocal* phenomena, such as optical activity. Indeed, studies of anisotropy properties of plasmon modes,[8–10] performed with different linear polarizations, do not show a dependence on the cluster size. One can find that the difference between p- and s-polarized incident light is given by

$$\Delta|d_{i\alpha}|^2_{p,s} = \sum_{n,m} n_{i\alpha} m^*_{i\alpha} C_n C^*_m \sum_{j,l} \exp[-\gamma(z_j + z_l)] \times (n_{jz} m^*_{ly} - n_{jy} m^*_{lz}) \times \cos k_x (x_j - x_l)(E_0^2/2). \quad (10)$$

In this case the difference in dipole distribution depends on $\cos k_x(x_j - x_l)$ so that a strong polarization dependence can and does occur even if the cluster size is much less than λ. This conclusion is in agreement with numerical simulations,[6–8] where a high sensitivity of the dipole distribution to a change in linear polarization was shown even for the case when the cluster size R_c was much less than the wavelength.

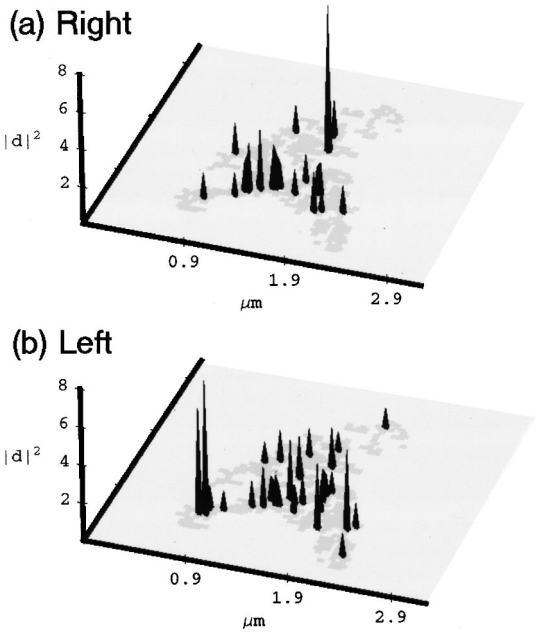

Fig. 8. Numerical simulations for the dipole-moment distribution (arbitrary units) for model fractal cluster of $N = 5000$ particles, for (a) right- and (b) left-circular polarizations of the incident light ($\lambda = 800$ nm). Each simulated image is 3 μm × 2 μm in size.

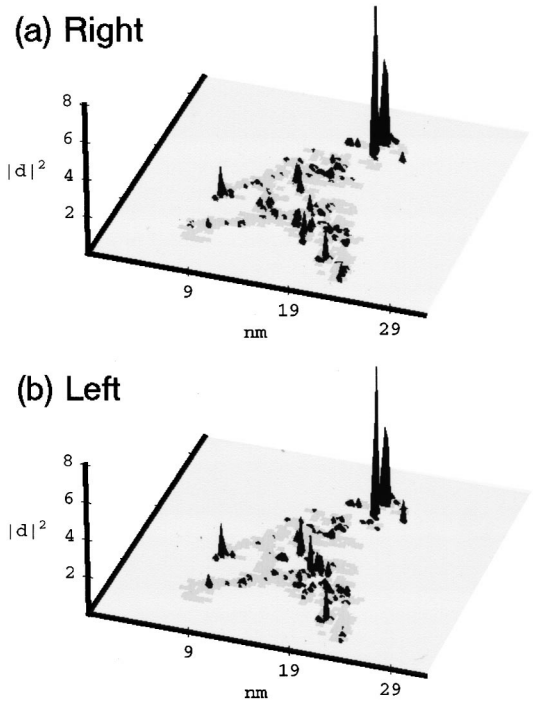

Fig. 9. Same as Fig. 8 except that the fractal cluster size is reduced by 100 times. Each simulated image is 30 nm × 20 nm in size. The incident light wavelength remains at $\lambda = 800$ nm.

The field-intensity distributions above a sample for right- and left-circular polarized incident waves were simulated for comparison with our experiments. The field at an arbitrary point $\mathbf{r}$ created by a set of dipoles in Eq. (6) can be written as

$$E_{\alpha,R,L}(\mathbf{r}) = \sum_n f_{n\alpha}(\mathbf{r})(\bar{n}|\,\sigma_{R,L})E_0. \quad (11)$$

The mode weight distribution $f_{n\alpha}(\mathbf{r})$ is given by

$$f_{n\alpha}(\mathbf{r}) = \sum_i G_{\alpha\beta}(\mathbf{r} - \mathbf{r}_i)(i\beta|n)C_n\,, \quad (12)$$

where $G_{\alpha\beta}(\mathbf{r} - \mathbf{r}_i)$ is the regular part of the free-space dyadic Green's function.

The differential scattered intensity is given by $\Delta I_{R,L} = |E_R(\mathbf{r})|^2 - |E_L(\mathbf{r})|^2$. It can be shown that

$$I_{R,L} = (E_0^2/4)\sum_{m,n}\left\{ f_{n\alpha} f^*_{m\alpha} \sum_{j,l} [(n_{jy} m^*_{ly} + n_{jz} m^*_{lz}) \times \cos k_x(x_j - x_l) \pm (n_{jz} m^*_{ly} - n_{jy} m^*_{lz}) \sin k_x(x_j - x_l)] \times \exp[-\gamma(z_j + z_l)] \right\}. \quad (13)$$

Because $k_x = k \sin\theta$, CIDS depends on the angle of incidence θ. Thus the difference $I_R - I_L$ is proportional to

$\sin k_x(x_j - x_l)$ so that the main contributions to CIDS come from the mode amplitudes separated by distances comparable with the wavelength. It means that the local CIDS is sensitive to a long-range distribution of resonant and anisotropic modes (with the anisotropy characterized by the $(n_{jz}m^*_{ly} - n_{jy}m^*_{lz})$ factor).

Figure 10 plots PSTM images calculated by numerically solving the CDEs, with the formalism described above. The finite acceptance distance and acceptance angle of the fiber tip were taken into account in these simulations. In agreement with experimental observations, the hot-spot locations are different for different circular polarizations. The distribution for the local CIDS parameter, $S_{14}/S_{11} = (I_R - I_L)/(I_R + I_L)$, is shown at the bottom; it clearly exhibits large local optical activity.

Thus experiment and theory both provide evidence that hot spots in fractals may be optically active, with $|(I_R - I_L)/(I_R + I_L)| \approx 0.5$. The difference in optical response to different circular polarizations occurs because the fractal modes may have different projections $(\bar{n}|\sigma_{R,L})$ on the helical configuration of the incident field with opposite signs of helicity. In other words, spatial distribution of a fractal eigenmode can have certain handedness and, in that sense, it possesses chirality. As mentioned, the mode chirality occurs because local structures in a fractal typically have neither center nor plane of symmetry. The observed difference between $I_R(\mathbf{r})$ and $I_L(\mathbf{r})$ means that different (and spatially separated) modes with opposite signs of handedness may be in resonance with the field of the same frequency. The set of resonating modes is defined by the condition $\mathrm{Re}[1/\alpha_0 + v_n] \leqslant \gamma_n$, where γ_n is the resonance width. A change in the wavelength leads to another set of resonant modes excited by the incident field. If the new set contains eigenmodes with different projections $(\bar{n}|E)$, it may result in a change in the magnitude (and even the sign) of the differential optical response, in accord with Fig. 7(a).

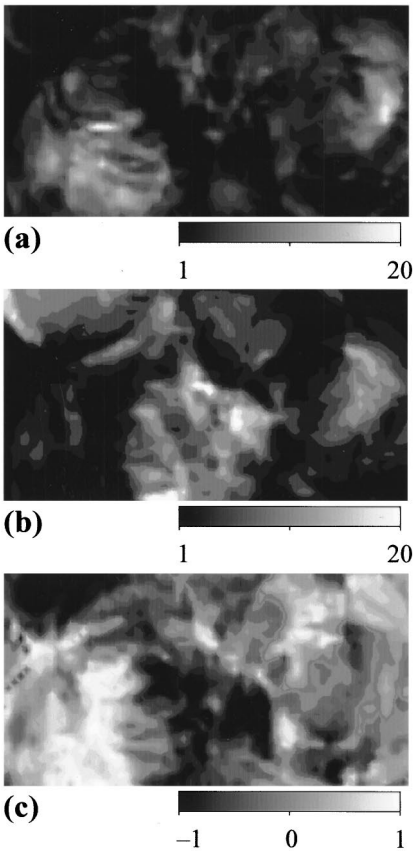

Fig. 10. Numerical simulations for the scattered light at a height of 2 μm above a silver fractal aggregate for (a) right- and (b) left-circular polarizations of the incident light (λ = 800 nm) and (c) for the CIDS parameter. Each simulated image is 2 μm × 1 μm in size.

We note that the macroscopic optical activity of conventional chiral objects is usually much less than one due to the Boltzmann–Kuhn factor, which is the ratio of molecular size to the light wavelength. In contrast, the local CIDS in fractals is of the order of one, which is the theoretical maximum. Furthermore, the local CIDS occurs in hot spots, where the local fields exceed the applied field by large factors.

4. CONCLUSION

In conclusion, giant *local* optical activity in scattering has been observed in fractals formed by nongyrotropic particles, while these fractals have very small or zero *macroscopic* gyrotropy. We note that the observed effect is probably not limited to fractals; e.g., it can occur in random media, where electromagnetic excitations may experience Anderson localization on different local structures, many of which can have handedness. Thus local gyrotropy is anticipated to be a generic phenomenon in random media.

ACKNOWLEDGMENTS

We are grateful to participants of the seminar led by S. G. Rautian for helpful comments and A. K. Sarychev for useful discussions. This work was supported in part by the National Science Foundation under grants DMR-9810183 and DMR-0071901, the Army Research Office under grant DAAG55-98-1-0425, NASA under grants NAG8-1710 and NCC-1-01049, the Petroleum Research Fund under grant 35028-AC5, New Mexico Universities Collaborative Research of Los Alamos National Laboratory, Civilian Research and Development Foundation under grant RE1-2229, and the Russian Foundation for Basic Research under grant 99-02-16670.

*Also at Institute of Semiconductor Physics, Novosibirsk 630090, Russia.

†Present address: Celion Networks, Inc., Richardson, Texas 75082.

††Also at Institute of Automation and Electrometry, Novosibirsk 630090, Russia.

†††Also at School of Electrical and Computer Engineering, Purdue University, West Lafayette, Indiana 47907.

REFERENCES

1. V. M. Shalaev and M. I. Stockman, "Optical properties of fractal clusters (susceptibility, giant scattering by impurities)," Sov. Phys. JETP **65**, 287–294 (1987).
2. V. A. Markel, L. S. Muratov, M. I. Stockman, and T. F. George, "Theory and numerical simulation of optical prop-

erties of fractal clusters," Phys. Rev. B **43**, 8183–8195 (1991).
3. M. I. Stockman, L. N. Pandey, L. S. Muratov, and T. F. George, "Giant fluctuations of local optical fields in fractal clusters," Phys. Rev. Lett. **72**, 2486–2489 (1994).
4. V. P. Safonov, V. M. Shalaev, V. A. Markel, Yu. E. Danilova, N. N. Lepeshkin, W. Kim, S. G. Rautian, and R. L. Armstrong, "Spectral dependence of selective photomodification in fractal aggregates of colloidal particles," Phys. Rev. Lett. **80**, 1102–1105 (1998).
5. W. Kim, V. P. Safonov, V. M. Shalaev, and R. L. Armstrong, "Fractals in microcavities: giant coupled, multiplicative enhancement of optical responses," Phys. Rev. Lett. **82**, 4811–4814 (1999).
6. V. M. Shalaev, *Nonlinear Optics of Random Media: Fractal Composites and Metal–Dielectric Films* (Springer, Berlin, 1999).
7. M. I. Stockman, "Inhomogeneous eigenmode localization, chaos, and correlations in large disordered clusters," Phys. Rev. E **56**, 6494–6507 (1997).
8. D. P. Tsai, J. Kovacs, Z. Wang, M. Moskovits, V. M. Shalaev, J. S. Suh, and R. Botet, "Photon scanning tunneling microscopy images of optical excitation of fractal metal colloid clusters," Phys. Rev. Lett. **72**, 4149–4152 (1994).
9. S. I. Bozhevolnyi, V. A. Markel, V. Coello, W. Kim, and V. M. Shalaev, "Direct observation of localized dipolar excitations on rough nanostructured surfaces," Phys. Rev. B **58**, 11441–11447 (1998).
10. V. A. Markel, V. M. Shalaev, P. Zhang, W. Huynh, L. Tay, T. L. Haslett, and M. Moskovits, "Near-field optical spectroscopy of individual surface-plasmon modes in colloid clusters," Phys. Rev. B **59**, 10903–10909 (1999).
11. I. I. Smolyaninov, D. L. Mazzoni, and C. C. Davis, "Imaging of surface plasmon scattering by lithographically created individual surface defects," Phys. Rev. Lett. **77**, 3877–3880 (1996).
12. I. I. Smolyaninov, A. V. Zayats, and C. C. Davis, "Near-field second harmonic generation from a rough metal surface," Phys. Rev. B **56**, 9290–9293 (1997).
13. V. P. Drachev, S. V. Perminov, S. G. Rautian, and V. P. Safonov, "Giant nonlinear optical activity in an aggregated silver nanocomposite," JETP Lett. **68**, 651–656 (1998).
14. L. D. Barron, *Molecular Light Scattering and Optical Activity* (Cambridge University, Cambridge, UK, 1982).
15. W. D. Bragg, V. P. Safonov, W. Kim, K. Banerjee, M. R. Young, J. G. Zhu, Z. C. Ying, R. L. Armstrong, and V. M. Shalaev, "Near-field optical studies of local photomodification in nanostructured materials," J. Microsc. (Oxford) **194**, 574–577 (1999).
16. P. C. Lee and D. Meisel, "Adsorption and surface-enhanced Raman of dyes on silver and gold sols," J. Phys. Chem. **86**, 3391–3395 (1982).
17. B. Hecht, H. Bielefeldt, Y. Inouye, D. W. Pohl, and L. Navotny, "Facts and artifacts in near-field optical microscopy," J. Appl. Phys. **81**, 2492–2498 (1997).
18. S. I. Bozhevolnyi, "Topographical artifacts and optical resolution in near-field optical microscopy," J. Opt. Soc. Am. B **14**, 2254–2259 (1997).
19. P. Zhang, "Development of a near-field scanning optical microscope and its application in studying the optical mode localization of self-affine Ag colloidal films," Ph.D. dissertation (University of Toronto, Toronto, Canada, 1997).
20. S. I. Bozhevolnyi, "Localization phenomena in elastic surface-polariton scattering caused by surface roughness," Phys. Rev. B **54**, 8177–8185 (1996).
21. C. Bohren and D. Huffman, *Absorption and Scattering of Light by Small Particles* (Wiley, New York, 1983).
22. Yu. E. Danilova, V. A. Markel, and V. P. Safonov, "Absorption of light by random fractal cluster," Atmos. Oceanic Opt. **6**, 1436–1446 (1993).
23. V. A. Markel, V. M. Shalaev, E. B. Stechel, W. Kim, and R. L. Armstrong, "Small-particle composites. I. Linear optical properties," Phys. Rev. B **53**, 2425–2436 (1996).
24. V. A. Markel, V. M. Shalaev, and T. F. George, "Some theoretical and numerical approaches to the optics of fractal smoke," in *Optics of Nanostructured Materials*, V. A. Markel and T. F. George, eds. (Wiley, New York, 2000), pp. 355–412.
25. V. A. Markel, "Antisymmetrical optical states," J. Opt. Soc. Am. B **12**, 1783–1791 (1995).